Nanoscale cuticle mass density variations influenced by pigmentation in butterfly wing scales

Deepan Balakrishnan [1,2,7], Anupama Prakash[1,6,7], Benedikt J. Daurer [3,7], Cédric Finet[1], Ying Chen Lim [2,4], Zhou Shen [2,4], Pierre Thibault[5], Antónia Monteiro [1] ✉ & N. Duane Loh [1,2,4] ✉

How pigment distribution influences the cuticle density within a microscopic butterfly wing scale, and how both impact each scale's final reflected color, remains unknown. We use ptychographic X-ray computed tomography to quantitatively determine, at nanoscale resolutions, the three-dimensional mass density of scales with pigmentation differences. By comparing cuticle densities between two pairs of scales with pigmentation differences, we determine that the density of the lower lamina is inversely correlated with pigmentation. In the upper lamina structure of *Junonia orithya* and *Bicyclus anynana*, low pigment levels also correlate with sheet-like chitin structures as opposed to rod-like structures. Within each scale, we determine that the lower lamina in all scales has the highest density, and distinct layers within the lower lamina help explain reflected color. We hypothesize that pigments, in addition to absorbing specific wavelengths, can affect cuticle polymerization, density, and refractive index, thereby impacting reflected wavelengths that produce colors.

A detailed examination of the distribution of various matrix components within complex biological materials has often led to a better understanding of their color and other material properties[1–3]. Some of the main components found in arthropod cuticles are lipids, chitin fibers embedded in a matrix of cuticular proteins and tyrosine-derived pigment molecules, secreted by the underlying cells[4–7]. Variations in the chemical composition of these molecules and their organization within the layered matrix affect the properties and structure of the cuticle[6,8–14]. However, in the case of microscopic butterfly wing scales, which are the cuticular skeletons of single cells, little work has been done to explore how cuticle composition varies with scale morphology and color.

Arthropod cuticles are multi-layered, hierarchically organized structures[4,5]. Various layers are synthesized sequentially, with the outer epicuticular layers composed of lipids and proteins, while the inner procuticle layers are made of chitin and various proteins[15]. Chitin fibers are organized into diverse morphologies in cuticles of various natural systems[16,17] and their organization and interactions with other molecules can change within different parts of the same structure[16,18,19]. Chitin fiber organization can also change by modifications of the fibers such as deacetylation of chitin[20]. As in other cuticular structures, butterfly scale cuticles are similarly composed of multiple layers with different material compositions[21].

Butterfly scales owe their brilliant colors to either pigments in the cuticle[22,23] or the way that cuticle is patterned during development to produce non-pigmentary structural colors through light interference and diffraction[24,25]. As the scale grows, cuticle is secreted to the outside

[1]Department of Biological Sciences, National University of Singapore, Singapore, Singapore. [2]Centre for Bioimaging Sciences, National University of Singapore, Singapore, Singapore. [3]Diamond Light Source, Harwell Science & Innovation Campus, Didcot, UK. [4]Department of Physics, National University of Singapore, Singapore, Singapore. [5]Università degli Studi di Trieste, Trieste, Italy. [6]Present address: Centre for Engineering Biology and Department of Bioengineering, Imperial College London, London, UK. [7]These authors contributed equally: Deepan Balakrishnan, Anupama Prakash, Benedikt J. Daurer. ✉e-mail: antonia.monteiro@nus.edu.sg; duaneloh@nus.edu.sg

of the cell membrane to initially define two main cuticular surfaces: an upper lamina that is often intricately nanostructured, and a flat, sheet-like lower lamina (Fig. 1A)[24,26]. Over time, the upper lamina is further sculpted into various sub-structures, forming longitudinal ridges first, followed by cross-ribs[27]. Lastly, the two laminas are connected by pillars or trabeculae that form towards the end of development[27,28]. Pigmentation only begins at the late stages of scale development[23,29].

Both upper and lower laminas of the scale can produce structural colors, but variations in just the lower lamina thickness are often sufficient to produce a large range of colors via thin-film interference[30]. It has recently become apparent, however, that optical models that predict structural colors from the physical dimensions of cuticle alone, assuming a homogeneous chitin matrix, are failing to capture the true color of the scales[30]. In addition, investigations into the genetics of butterfly scale development have identified a complex interplay between scale morphology and pigmentation[30–32]. Pigments, such as melanins, are often deposited in the cuticular mass of the scale, and knockouts of two melanin pathway genes in *Bicyclus anynana* butterflies led to decreased pigmentation levels in wing scales but also impacted scale structures[31]. In *yellow* crispants, an ectopic cuticular film was retained in the upper structures of black scales, closing the normally open 'windows' (Fig. 1A, E), whereas in *Dopa Decarboxylase* (*DDC*) crispants, sheet-like trabeculae extended between the two laminas in place of pillar-like trabeculae[31]. Similar interactions between scale structure and coloration were observed in *Junonia* butterflies, where *Optix* crispant cover scales changed from brown to blue with a simultaneous decrease in pigmentation and an increase in the lower lamina thickness[30].

To better understand the influence of material composition on butterfly scale structure and their macroscopic optical properties, we require a 3D density map of the entire scale's structure at nanometer resolution with the corresponding color response that can be overlapped with the structure. However, there is no single imaging tool that can provide that. Various imaging modalities provide unique insights into the scale at different resolutions. Optical microscope images show us the color response, and a microspectrophotometer measures the reflectance and the absorbance spectra, but only with a few micrometers of resolution. Resin-section transmission electron microscopy (TEM) has a high sub-nanometer resolution that is adequate to resolve multilayers in the lower lamina, but due to heavy ion staining, the quantitative density estimation is not feasible. Optical modeling can combine the multilayers observed in the TEM images with the reflectance and absorbance measurements to suggest variations in material composition. Nevertheless, the absorbance measurement corresponds to total pigmentation and not pigment density.

Ptychographic X-ray computed tomography (PXCT) fills this gap by providing 3D mass density estimates through the collection of coherent diffraction patterns at overlapping scan positions across the specimen. The overlapping nature of the scans enables robust phase retrieval, which encodes fine structural details by recovering high spatial frequencies. Bright synchrotron sources, such as the Diamond Light Source, offer highly coherent and intense X-ray beams, enabling PXCT to achieve a few tens of nanometers resolution. Thus, PXCT can provide an intermediate resolution between the high-resolution TEM cross-sections and the low-resolution color response[33–37].

By utilizing a range of techniques from microspectrophotometry, scanning and transmission electron microscopy (SEM/TEM) to PXCT, we characterized how relative pigmentation differences are related to mass density distributions within different scale sub-structures, and their effects on scale color. In particular, we demonstrate the application of PXCT for estimating quantitative mass densities of scale sub-structures at nanoscale resolution. These measurements revealed density differences between the two laminas of the scale. In addition, the 3D structural measurements from PXCT enable the estimation of the absorption coefficient from the absorbance measurements that

correspond to the pigment density. Further, distinct layers within the lower lamina suggest that cuticle heterogeneity within the scale might affect how light travels through or bounces off cuticular surfaces. A multi-layered optical model taking into account these compositional variations in the lower lamina predicts the experimental reflectance spectra of the scale more accurately than models based on a homogeneous cuticle matrix. Finally, the local tilt measurements of the lower lamina from PXCT correlating with the optical microscope images explain the spatial color variations in the scale and show the influence of the upper lamina structure in homogenizing the color.

Results

Pigment distribution is similar between the upper and lower laminas of all scale types

In this study, we compared two pairs of scales with differences in pigmentation in two species of nymphalid butterflies, *Junonia orithya* and *Bicyclus anynana*. In *J. orithya*, we compared the less pigmented blue cover scales of males with more pigmented brown female scales sampled from the same site (Fig. 1B, D, and S1A, B). Similarly, in *B. anynana*, we compared cover scales from the *yellow* mutant line with the more pigmented black cover scales of wildtype, sampled around the large eyespot (Fig. 1C, E and S1C, D).

To determine the distribution of pigments between each scale's upper and lower laminas, we measured the reflectance and absorbance of single intact scales relative to scales with the upper laminas removed (Supplementary Data 1). Removing the upper lamina is beneficial, as the upper and lower laminas contribute differently to the total reflectance spectra. The lower lamina produces specular thin-film interference, and the upper lamina structures produce diffuse reflection (Lambertian reflection), so the optical responses can be inferred better by measuring the reflectance with and without the upper laminas. The upper laminas were scraped off with a pin, and the debris was removed using sticky tape (Fig. 1F). The epi-illumination image shows that the color response of the lower lamina is not affected by the removal process, and the SEM image shows that there is no residue left (Fig. 1F). The absorbance spectrum is affected by the scale's thickness and the density of color-absorbing pigments it contains. The thickness distributions of the upper and lower lamina from SEM and PXCT measurements (described below) enabled us to additionally estimate the absorption coefficient spectra (Figs. 1D″, E″, S2), which is related to the pigment density (see "Methods"). Here, pigment density refers to the amount of pigment per unit volume, and this should not be confused with the cuticle mass density, i.e., the total mass of chitin and pigment per unit volume.

The reflectance of all scale types increased upon removal of the upper lamina (Fig. 1D′, E′) while the absorbance decreased (Fig. S1E, F). However, the absorption coefficient was similar between the upper and lower laminas (Fig. 1D″, E″). This indicated that the density of light-absorbing pigments was similar between the two surfaces for each scale type.

Pigmentation correlates with changes in scale morphology

To assess scale structural changes associated with changes in pigmentation levels in all four scales, we measured inter-ridge and cross-rib spacing, and the thickness of the lower lamina, using a combination of SEM and FIB-SEM (Fig. S3, Supplementary Data 2). The blue scales of *J. orithya* males differed from the highly pigmented brown scales of females by having greater inter-ridge (linear mixed effects model (lme), chisq = 336.12, p-value < 0.001) and cross-rib distances (lme, chisq = 331.89, p-value < 0.001), leading to larger 'windows' on the upper lamina (Fig. S3A, B). In addition, the blue scales had a thicker lower lamina of ~190 nm as compared to the thinner lower lamina of ~158 nm in the brown scales (t-test, t(4) = 8.12, p < 0.001) (Fig. S3C). This thicker, thin film of males produced a structural blue via constructive interference[30].
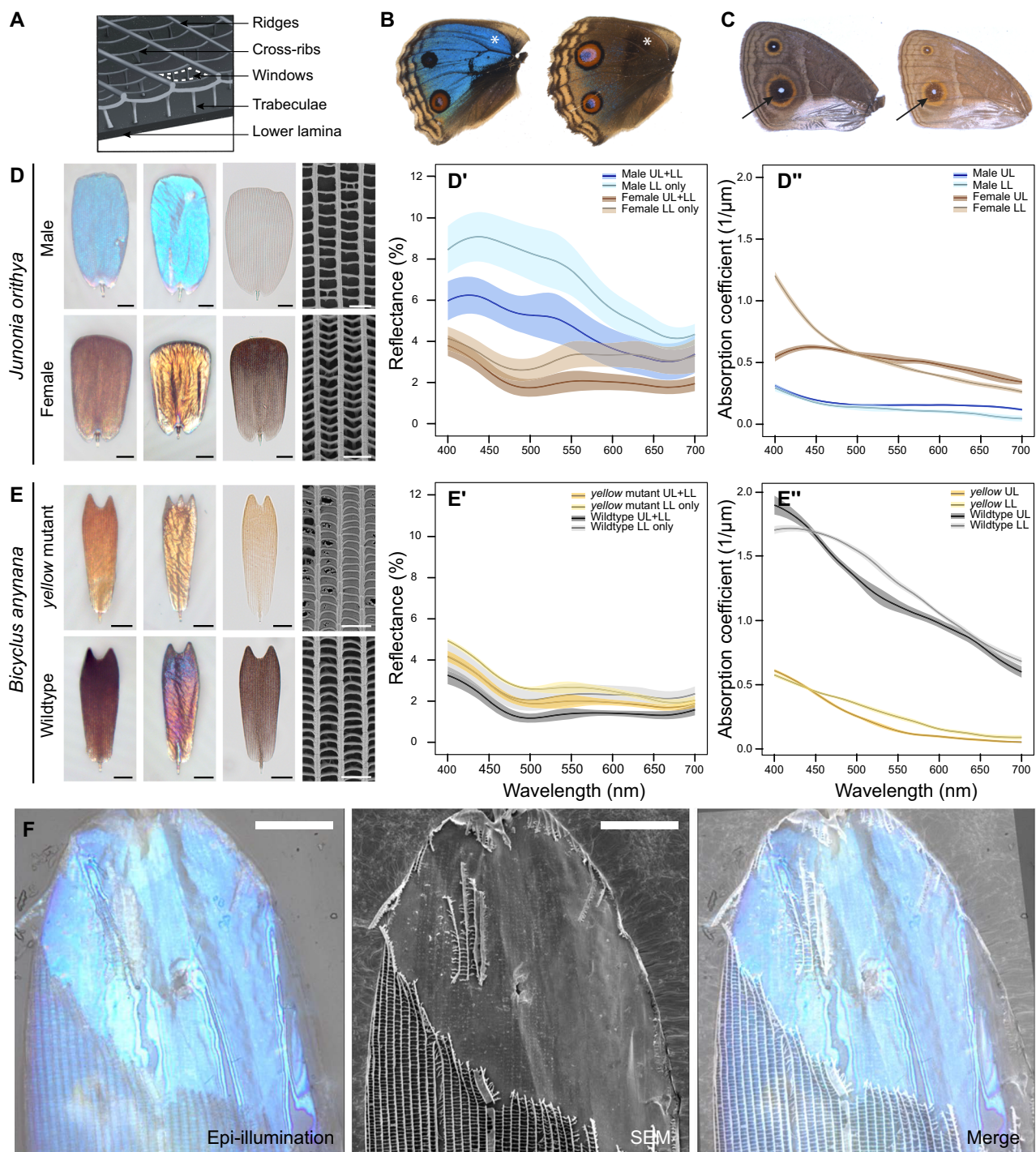
Fig. 1 | Reflectance and absorption profiles of *Junonia orithya* and *Bicyclus anynana* scales. A Schematic of a wing scale showing a typical scale structure (digitally illustrated in Procreate). B Dorsal hindwings of a *J. orithya* male (left) and female (right). White stars indicate the regions sampled. C Ventral forewings of a *B. anynana* wildtype (left) and *yellow* mutant (right). Black arrows indicate the regions sampled. D, E Optical and SEM images of a male blue scale and a female brown scale of *J. orithya* (D), and a *yellow* mutant scale and wildtype scale of *B. anynana* (E). First column: Abwing images; Second column: Adwing images; Third column: Optical microscopy images of scales immersed in a chitin refractive index matching liquid that eliminates structural colors and measures pigmentary colors; The interference pattern in *J. orithya* male scale immersed in a chitin refractive index matching liquid is caused by an imaging artifact called color Moire. This is caused due to downsampling an image with a periodic structure to a smaller number of pixels in Fig. 1.

Fourth column: SEM images of the upper lamina structures. Scale bars for the optical images are 20 μm and the SEM images are 2 μm. (D′, E′) Reflectance spectra (Solid curve = mean spectrum; shaded band = ± 1 SD (standard deviation)) of abwing *J. orithya* (D′) and *B. anynana* (E′) scales with intact upper and lower laminas (UL + LL) and scales with the upper laminas removed physically (LL only). (D″, E″) Estimated absorption coefficient spectra of *J. orithya* (D″) and *B. anynana* (E″) scales for their upper laminas (UL only) and lower laminas (LL only). At least three scales have been imaged from 2 different individuals; the exact sample sizes and replicate types for each curve are detailed in the 'UV-VIS-NIR microspectrophotometry' subsection of "Methods". Source data for panels D′, E′, D″, and E″ are provided in Supplementary Data 1. (F) An illustrative example of a *J. orithya* blue scale with the upper lamina removed, imaged under epi-illumination, scanning electron microscopy (SEM), and a merge of the two. The scale bars in (F) are 20 μm.

Among the *B. anynana* pair of scales, the *yellow* mutant scales displayed an ectopic cuticular film on the upper lamina closing all the windows (Fig. 1E). TEM cross-sections indicated that the film was a very thin cuticle layer of about 10–20 nm in thickness (Fig. S4). These *yellow* mutant scales also had larger inter-ridge distances (lme, chisq = 12.91, *p*-value < 0.001) and a denser arrangement of cross-ribs (lme, chisq = 10.82, *p*-value < 0.001) relative to wildtype scales, as reported previously in ref. 21 (Fig. S3A, B). The thickness of the lower lamina of the *B. anynana* wildtype scales was similar to the *yellow* mutant scales based on FIB-SEM measurements (*t*-test, t(4) = 1.31, *p*-value = 0.23) (Fig. S3C).

To probe the distribution of materials within the scale substructures at nanoscale resolution, we imaged one scale for all four scale types using ptychographic X-ray computed tomography (PXCT). A cryo-PXCT has been reported on a beetle scale to achieve a 3D resolution of 28 nm over a small sample volume of $7 \times 7 \times 7 \mu m^3$ [37]. Here, we employed PXCT over much larger volumes of $70 \times 35 \times 35 \mu m^3$ with a 3D resolution of 66.5 nm. The PXCT reconstructions provided 3D distributions of electron densities (Fig. 2; see "Methods", Supplementary Movies 1-4)[26,33]. The 3D electron density maps showed both changes in density between upper and lower laminas as well as morphology between the pigmented and less pigmented scales of each species (Fig. 2). In both *J. orithya* and *B. anynana* scales, the upper lamina of the less pigmented scale had sheet-like extensions from the cross-ribs as compared to the rod-like cross-ribs in the more pigmented scale (Fig. 2 and S5, 6). The *B. anynana yellow*
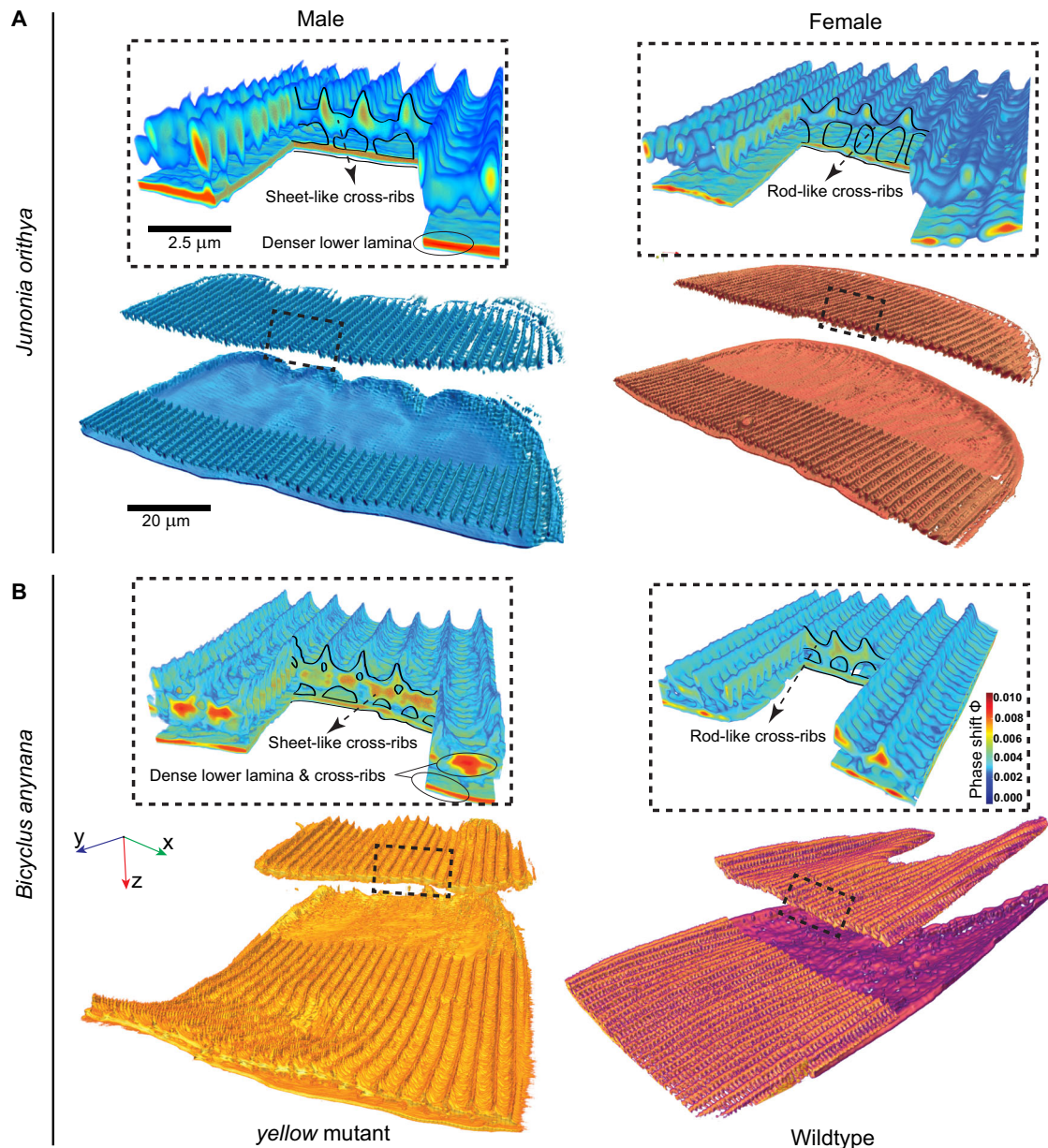

Fig. 2 | Volume segmentation of 3D PXCT reconstructions of *J. orithya* and *B. anynana* scales. False color density contour renders of a (**A**) *J. orithya* male blue scale (left), and a female brown scale (right); and (**B**) a *B. anynana yellow* mutant scale (left) and a wildtype scale (right). The renders show digitally separated upper laminas cut out from the rest of the scales. Black, dashed rectangles indicate the regions magnified for 3D electron density maps of the upper and lower lamina. Cross-sections along the ridges and across the ridges in the 3D heat maps show electron density variations within the scales. Annotated black lines outline the structural differences across scales. The figure shows that the PXCT reconstructions provide 1) 3D structural data over a large field of view, 2) nano-scale density information of the specimen, and 3) digital segmentation of the reconstructed volume to estimate density variations of each sub-structure in a physically intact scale.

mutant scale also had disordered and bent trabeculae (Figs. S6B, S7), that are not seen in the wildtype scale (Figs. S6A, S7). Decreased pigmentation correlating with sheet-like cross-ribs suggests that the concentration and the type of pigments may determine structural differences between the scales, i.e., rod-like or sheet-like cross-ribs and straight or bent trabeculae, by modulating chitin polymerization.

Cuticle mass density is highest in the lower lamina within a scale, and the lower lamina of scales with less pigmentation have higher mass density

To understand how the mass distribution varied between the different sub-structures of each scale, we computationally rotated and segmented the PXCT volumes into upper and lower laminas, and then the upper lamina was further clustered into the three sub-structures: cross-ribs, ridges, and trabeculae based on their column-wise (z-axis) 1D mass density profiles (Fig. 3A–D) (details in the step-by-step procedural description of mass density estimation section of Methods). Each such 1D profile shows the variation of mass densities along the abaxial-adaxial axis (top to bottom surface) of the scale, measured as voxels along the z-axis (Fig. 3A–D, inset). We segmented and classified these 1D profiles as lower lamina, ridges, cross-ribs, trabeculae, or ectopic film on the upper lamina (for *yellow* scales) and calculated a boxplot of average mass densities within each structural class for the four scale types (Fig. 3A'–D'). The mass densities within these sub-structures were calculated assuming each was made of only chitin since their cuticular protein, lipid and pigment compositions are unknown. Hence this would provide us a lower bound for the density estimates; a similar estimate based on melanin will increase the density values by ~11% (details in the segmentation and mass density estimation section of Methods). The contour-labels on the 2D density maps (scales seen from the top) validate the structural classification (Fig. 3A''–D''). The 1D mass density profiles shown in Fig. 3A–D represent the average 1D profiles of aligned and classified substructures from each scale type represented in Fig. 3A''–D''. Since the classification and the density estimation are determined from 10,000 1D mass density profiles for each scale type, the statistical inference is more robust against noise. We caution that while PXCT reliably shows the relative cuticular densities between and within scales, the absolute cuticle density estimates reported here are lower bounds, owing to the well-known underestimation of densities in tomography of thin samples[38].

The limited resolution (66.5 nm voxel side-length) and artifacts in the PXCT reconstructions of the complex architecture of the *yellow* mutant scale resulted in ambiguous class boundaries between the ectopic film on the upper lamina, cross-ribs, and trabeculae. In Fig. 3C, the inset arrows show the affected region in the 1D profiles that cause ambiguous class boundaries. Hence, the segmentation for this scale type was carried out based on the relative distance from the lower lamina. Further, we used double Gaussian fits to account for the presence of multiple substructures in a single 1D profile of the upper lamina (see "Methods"). The ambiguous regions were avoided in the density calculations and are represented as white regions in the density map (Fig. 3C''–D''). Moreover, because the short trabeculae under the cross-ribs were smaller than the voxel side-length of our PXCT reconstructions, these features were less apparent in both the *B. anynana* and *J. orithya* pairs of scales. Nevertheless, we determined the density from the trabeculae, ectopic film, and cross-ribs that are clustered unambiguously, as we have sufficient data points.

For the lower lamina, mass density was inversely correlated with pigmentation in both species. In all four scale types, the lower laminas were the densest sub-structures (Figs. 3A–D, 3A'–D' and 4), and scales with less pigmentation had higher lower lamina density.

For the upper lamina sub-structures, the relationship between density and pigmentation within each pair of scales was more complicated. In *B. anynana*, mass densities of the cross-ribs and trabeculae were higher in the lighter yellow mutant scale compared to the darker

wildtype scale (Fig. 3C', D'). However, the opposite was observed in the upper lamina of *J. orithya*, where cross-rib density was higher in the more pigmented female scale (Fig. 3B'). The ridges of the more pigmented scales in each scale-pair had higher mass densities in both *B. anynana* and *J. orithya* (Fig. 3).

PXCT's limited resolution impacted our mass density estimates. Recall that these densities were estimated from the Gaussian fits of the 1D z-profiles averaged within each sub-structure class identified using clustering of each scale. Since all the sub-structures (except the ectopic film, discussed below) are much larger in the z-axis (once rotated) than a single voxel (66.5 nm), this average density estimation along the z-axis is more robust against finite-volume effects than if we had estimated densities from single voxels (Fig. S8). Conversely, this finite-volume effect impacted mass density estimates of the thin ectopic film on the yellow mutant *B. anynana*'s upper lamina. These films, which were identified in the regions between the sheet-like cross-ribs (yellow contours in Fig. 3C''), were absent in the other three scale types in this study (Fig. 4). Since these ectopic films were less than one voxel thick (red dashed box in Fig. 3C'), they are more prone to finite-volume effects compared to other sub-structures, hence their mass density estimates were also more severely underestimated.

Overall, our PXCT reconstructions had sufficient resolution to compare the lower-bound estimates of mass densities across the prominent sub-structures. Nevertheless, with modestly higher resolution (e.g., 10 nm), PXCT would likely be able to resolve the ectopic film and even the density variations within each sub-structure.

Variation in cuticular composition within the lower lamina help to model blue structural color

Whereas our PXCT reconstructions indicated variation in cuticlar mass densities amongst different sub-structures of the scale, further compositional variations were observed in the high-resolution TEM resin-sections (pixel size 0.8 nm) of the lower lamina of the *J. orithya* male scale alone (Fig. 5A). Such multi-layered lower laminas have been observed in TEM sections of other butterfly species[39] and are likely related to the different cuticular layers such as epicuticle and procuticle made of different materials. Thayer and colleagues reported that the sub-200 nm thick lower lamina of blue butterfly scales should either be composed of a high refractive index material or require a more complex model to match the modeled and experimental reflectance spectra[30]. We confirmed that a single layer of chitin with refractive index 1.56 needs to be around 220 nm thick to match the observed blue reflectance spectra (Fig. S9A), which is far thicker than our SEM and TEM measurements (Fig. S3).

To understand how the compositional heterogeneity of the lower lamina impacts reflected color, we measured the reflectance spectra from regions of a blue scale from male *J. orithya* where we physically removed its upper lamina. The physical removal of the upper lamina leaves a planar lower lamina; the planar lower lamina of the male blue scales of *J. orithya* makes them a suitable candidate for modeling the reflectance spectrum (thin-film interference) to gain insights into the wavelength-dependent refractive index of the multiple layers within, similar to Leertouwer and colleagues[40]. We fitted the measured spectra with a four-layer lower-lamina model, which matches the measured broad-spectral reflectance better than a homogenous chitin slab model, a homogenous melanin slab model, and a homogenous slab model with an intermediate refractive index (Fig. 5B).

Our four-layer model accounted for the thickness variations in the lower lamina measured from SEM (Fig. S3), the thickness of distinct layers within the lower lamina from the TEM measurements (Fig. 5A), and the measured absorbance spectra (See Methods). Hence, only the scales with both the reflectance and the absorbance measurements are considered in the modeling (Fig. 5B). Since the scales are placed on a glass slide in our measurements, we included scattering from the glass substrate in our models (Fig. 5D).
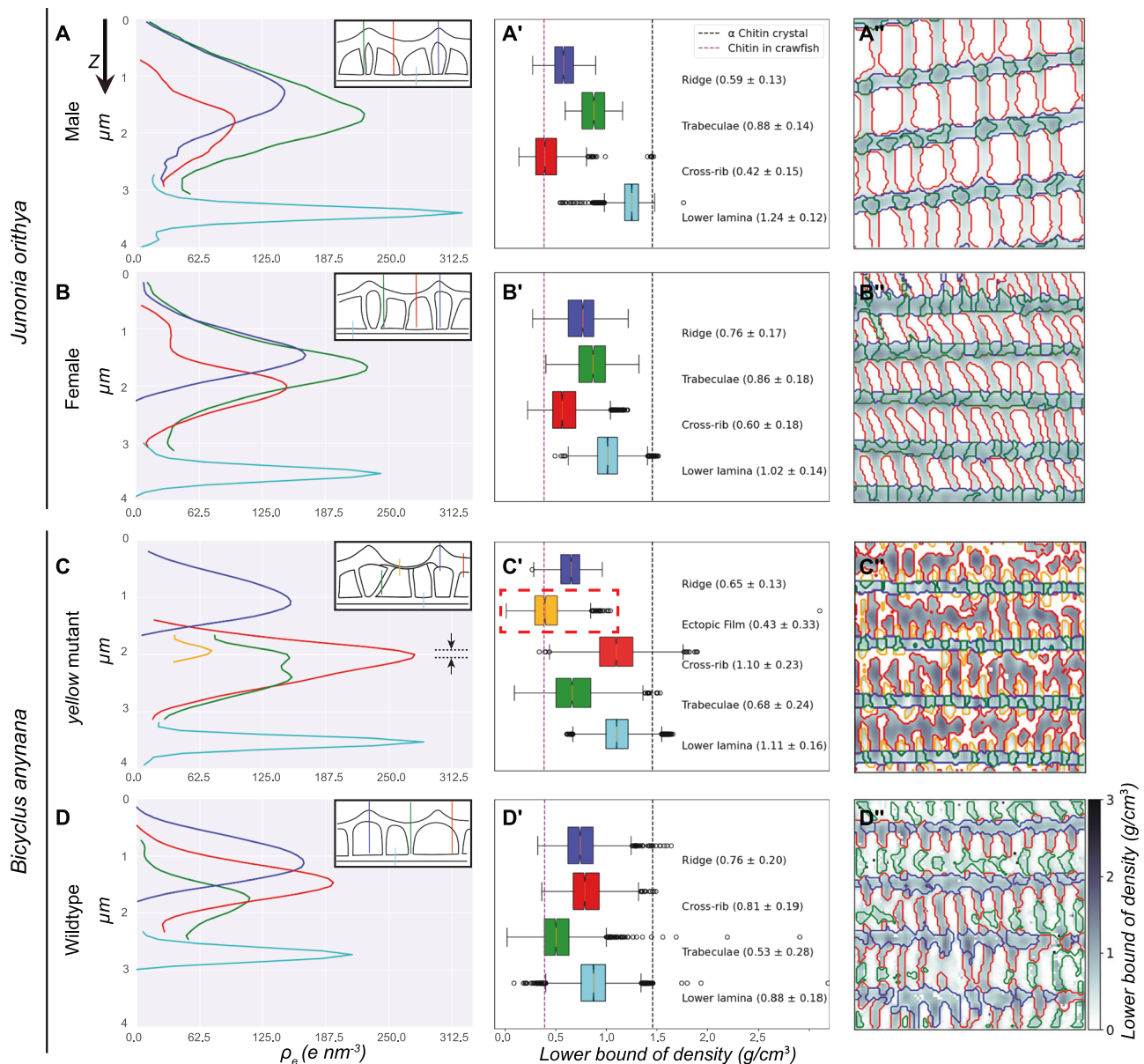
Fig. 3 | Mass density estimations from the segmented volumes of *Junonia orithya* and *Bicyclus anynana* scales. Sub-volumes from the PXCT reconstructions are segmented and clustered based on mass distribution (details in the step-by-step procedural description of the mass density estimation in Methods). (**A**–**D**) The mean electron density distribution along the z-axis (from abwing (upper) to adwing (lower)) of different upper lamina sub-structures with respect to the lower lamina of *J. orithya* male and female scales (**A**, **B**) and *B. anynana yellow* mutant and wildtype scales (**C**, **D**). Insets show a schematic view of the scales with colored lines marking the transected regions measured by the corresponding-colored curves. Cyan−lower lamina, red−cross-ribs, green−trabeculae, blue−ridges, and yellow−ectopic film. We can see from the insets that the lower lamina is further away (in the z-axis) from other upper lamina structures, which is why the cyan curves are well separated and do not overlap with the other curves. (**A′**–**D′**) Box plots (Center line = median; box = 25th–75th percentiles; whiskers = values within 1.5 × IQR;

points = outliers) of the estimated mass densities clustered as lower lamina, cross-ribs, ridges, and trabeculae reveal density variations across the scale sub-structures within each pair of differentially pigmented scales. Mass densities of α-chitin and chitin in crawfish are plotted to show the range of chitin densities reported in various organisms. The red dotted rectangle over the ectopic film density box plot in **C′** indicates that the density estimate is unreliable, as the ectopic layer thickness is significantly smaller than the voxel-resolution limit of the PXCT. Statistics are derived from one complete PXCT tomogram per scale type (one biological replicate), and 10,000 independent voxel-column measurements within the PXCT volume (technical replicates) are used to compute the density box plots. (**A″**– **D″**) 2D mass density maps (upper lamina only) of the sub-volumes identified with colored contours. Source data for this figure are available in Zenodo (10.5281/zenodo.12703866).

Variations in the thickness of the lower lamina, the angular incident light caused by the numerical aperture, and backscattering from the background/substrate can cause incomplete destructive interference such that the spectrum's minimum does not fall to zero (See "Methods", Fig. S9). Specular reflection from wing scales that are improperly calibrated to a diffuse standard can result in overestimated reflectance. Hence, it is a common but perhaps ambiguous practice to

subtract each measured spectra by an ad-hoc constant so that its resultant minima reaches zero, and divide this result by another ad-hoc correction factor to account for reflectance overestimation[30]. Since we included the glass substrate in the model, and instead used a mirror reference to calibrate the experimental spectra (see Methods, UV-VIS-NIR microspectrophotometry), we neither have to divide by a constant correction factor nor have to subtract for normalizing the spectra.
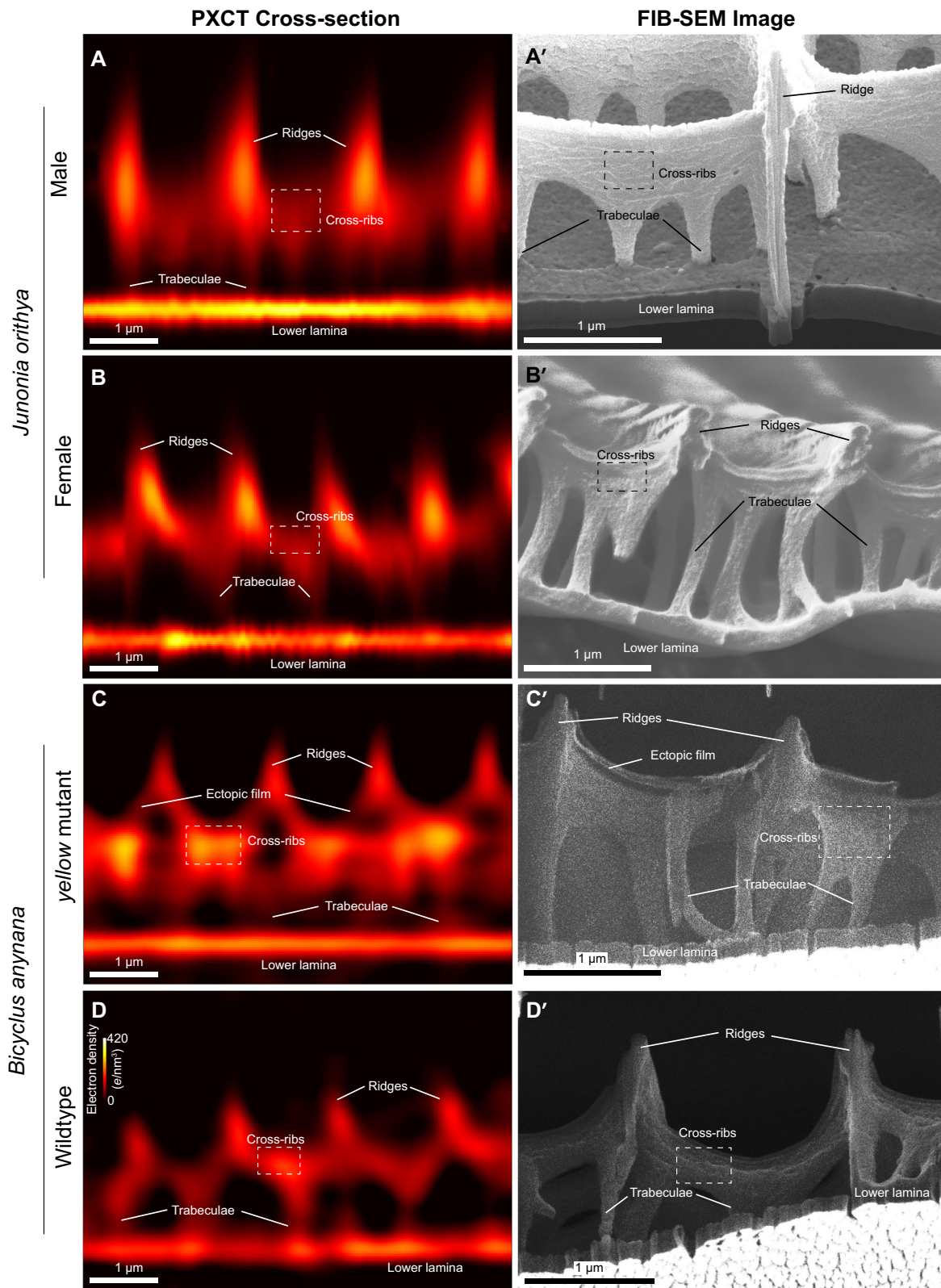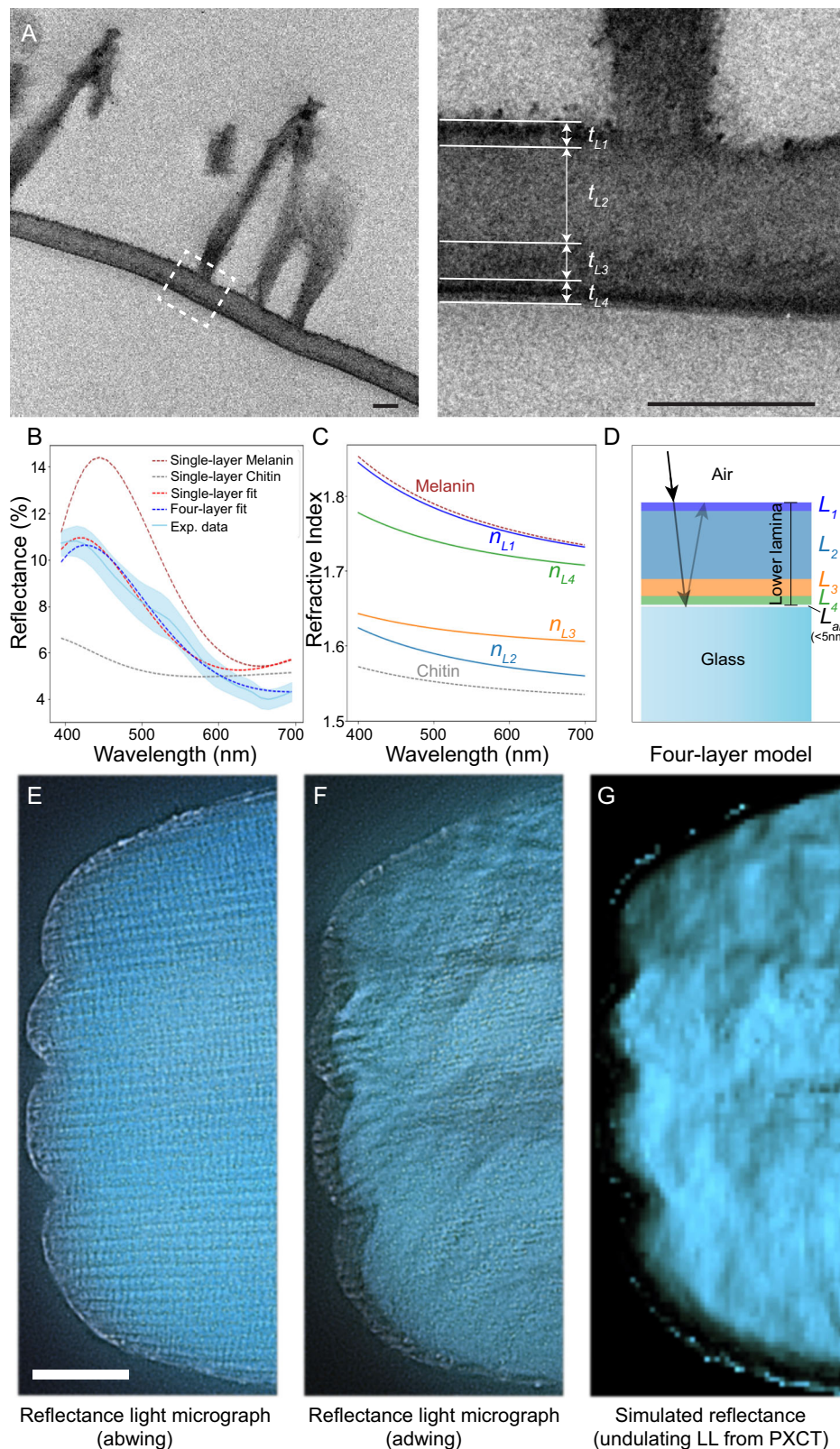
Fig. 4 | Comparison of PXCT cross-sections with the FIB-SEM images of *Junonia orithya* and *Bicyclus anynana* scales. (A–D) Cross-sections of the scales that are digitally cut from the PXCT reconstructions show the resolved structures and density distributions within the sub-structures. One PXCT tomogram per scale type. **(A′–D′)** FIB-SEM cross-sections of similar scales of each type. The traditional FIB-SEM images show structural similarity to the PXCT reconstructions. For *J. orithya*, 3-5 scales were imaged across 3 individuals. For *B. anynana*, 4 scales were imaged across 2 individuals.

Reflectance light micrograph
(abwing)

Reflectance light micrograph
(adwing)

Simulated reflectance
(undulating LL from PXCT)

Our models empirically accounted for the changes in refractive index n for different wavelengths of light λ using Cauchy's transmission equation ($n(\lambda) = A + B/\lambda^2$). While our four-layer model regressed for different Cauchy coefficients (A, B) for each layer, these fitted coefficients were constrained to respective values between those of pure chitin and pure melanin. The four-layer model more accurately captures the measured reflectance spectra than a single-layer model

and additionally enables inference of the spatial distribution of melanin-rich and chitin-rich regions within the lamina. The regressed Cauchy coefficients of each of the lower lamina layers from our model were: $A_{L1} = 1.677$, $B_{L1} = 2.68\cdot10^4$ nm², $A_{L2} = 1.529$, $B_{L2} = 1.52\cdot10^4$ nm², $A_{L3} = 1.588$, $B_{L3} = 8.84\cdot10^3$ nm², and $A_{L4} = 1.673$, $B_{L4} = 1.66\cdot10^4$ nm². The fitted refractive indices are higher for the top and bottom layers, corresponding to the darker TEM image layers (Fig. 5A). From our

Fig. 5 | A multi-layer thin-film interference model fit for reflectance spectra of *Junonia orithya* male blue scale. A TEM image of a blue scale of *J. orithya* male. The sample has not been stained with uranyl acetate or lead citrate; only osmium tetroxide is used for the postfixation. The white rectangle indicates the region cropped for the magnified view. The lower lamina shows two brighter layers sandwiched between the darker layers. The scale bar is 200 nm. The same four-layer contrast was observed in 12 images collected from 3 *J. orithya* male scales from 1 individual; layer thicknesses were quantified from the image shown here. **B** Experimentally measured reflectance spectrum of a *J. orithya* male scale (the upper lamina physically removed) placed on top of a glass slide, shown in light blue; solid curve represents the mean spectrum (shaded band = ± 1 SD) of six measurements from $n = 2$ independent scales. This spectrum is superimposed with four simulated spectra: a single 190 nm-thick layer of chitin placed on a glass slide using chitin's refractive index from unpigmented glassy scales; a single 190 nm-thick layer of melanin on glass using melanin's refractive index determined from bird barbules; a four-layer 190 nm-thick film on glass where the refractive indices in each layer are allowed to vary, and taking layer thicknesses from (**A**); a single 190 nm-thick layer thin film whose refractive indices are allowed to vary. The models account for a thin air gap with variable thickness; however, fitting results suggest its contribution is negligible. Source data for this panel are provided in Supplementary Data 1. **C** The wavelength-dependent refractive indices (Cauchy coefficients) of melanin, chitin, and the corresponding best-fit indices of the four layers of the lower lamina in the four-layer model in (**B**). **D** Schematic of four-layer model: four-layered lower lamina (L_1, L_2, L_3, and L_4) on top of a glass slide with a thin layer of air (L_{air}) between the lower lamina and the glass. **E, F** Epi-illumination light microscopy images of the abwing side (**E**) and the adwing side (**F**) of the same *J. orithya* male blue scale imaged with PXCT. The scale bar in panel E represents 20 μm and applies to panels (**E–G**). **G** A reflectance map was simulated using the four-layer model and an estimated tilt map of the lower lamina from the PXCT reconstruction. The local tilt affects the color and intensity response that correlates well with the adwing light microscopy image (**E**).

model, the refractive index of L1 approximately matches that of melanin rodlets in bird feather barbules[41], while that of L2 is closest to chitin (Fig. 5C).

We also noticed that spatial color variations were present within a single scale. To investigate which factors led to this, we first modeled overall scale color from the thin film interference reflectance and then subjected the same *J. orithya* male scale used in PXCT to high-resolution epi-illumination reflectance light microscope (Figs. 5E, F). First, we applied our optical parameters found in the four-layer model fit discussed above to the lower lamina's spatially varying local tilt map extracted from the PXCT reconstruction. Here we assumed a constant thickness in local directions perpendicular to the lower lamina; hence, the transverse variations of the lamina's apparent thickness as viewed from a fixed position either above or below the scale is entirely due to the lamina's changes in local tilt (i.e., undulations). We found that the simulated spatial variations in color reflectance across the scale's lower lamina (Fig. 5G), without the upper lamina, were very sensitive to the changes in this local-tilt-induced apparent thickness (Supplementary Movie 5 (GIF)). The upper lamina structures act as a color diffuser that spatially homogenizes the variations in color reflectance when viewed from the abwing direction (Fig. 5E). Overall, these results indicate that the lower lamina of the *J. orithya* blue scale is not a uniform thin film but an undulating, multi-layered structure composed of materials of different refractive indices that impact the resultant structural colors. The color is very sensitive to tilt and lamina thickness, but color is spatially homogenized by the light-diffusing sub-structures of the upper lamina[22,42].

Discussion

In this work, we looked at two pairs of butterfly scales that differ in levels of pigmentation to understand how pigments affect cuticular densities and scale structure. By calculating the absorption coefficient, we show that though the absorbance decreases when the upper lamina of a scale is removed, the pigment per unit volume is similar between the upper and lower laminas. The amount of pigments affects cuticular structures, especially the cross-ribs, where sheet-like cross-ribs occur in scales with lower pigment levels as compared to rod-like cross-ribs in darker scales. We then identify that the lower laminas of all four scale types had the highest mass densities, and this inversely correlated with pigmentation.

The mass density variations between the scales in each pair of comparisons may be due to differences in their material composition or how their constituent monomers pack together. Due to the sequential nature of multi-layered cuticle development and the late deposition of pigments, distinct scale sub-structures that develop at different times may have combinations of the various cuticle layers with different amounts of pigments. For example, the last sub-structure to develop i.e, the trabeculae, likely lacks the epicuticle

layer. Further, since pigments are deposited in scales during the late stages of development, the formation of the later sub-structures like the cross-ribs and trabeculae may be affected more by the presence of pigments.

The compositional heterogeneity of the lower lamina, seen in the TEM images and corroborated by our optical modeling, fits with the ordered deposition of various cuticle components. The darker regions in the TEM resin section (Fig. 5A and S10), are caused by the osmium stain that we used as a post-fixative during sample preparation. Osmium preferentially binds to unsaturated, double-bonded molecules such as lipids and proteins, and pigments like melanins[43,44]. We considered the possibility that the observed contrast of distinctive layers within the lower lamina could result from incomplete penetration of osmium tetroxide, as staining prior to sectioning may lead to stronger deposition near the outer surfaces. If the penetration of osmium were limited to the outer surfaces, we would expect a symmetric diffusion from both sides of the lower lamina. However, we observe an asymmetrical distribution of contrast, which indicates that limited osmium penetration alone does not account for the observed contrast. (Fig. 5A and S10). Additionally, the upper lamina structures exhibit strong and consistent staining throughout their thickness, suggesting that osmium tetroxide can penetrate the entire volume of the scale structure under our staining conditions (Fig. S10). Though we cannot entirely rule out some staining artifacts, our observations are likely dominated by preferential osmium binding to melanin-rich substructures rather than the misleading contrast arising solely from limited stain penetration.

In our model (Fig. 5D), the two darker layers (L1 and L4 in Fig. 5D, corresponding to thicknesses *t1* and *t4* in Fig. 5A) had higher refractive indices that are close to that of melanin's. We therefore speculate that the innermost layer L1 (closer to the trabeculae) contains melanins while the outer layer L4 is lipid- and protein-rich either with or without small amounts of melanins. The other two layers had lower refractive indices, closer to chitin, suggesting they might be the protein-rich (L3; Fig. 5A) and the chitin-protein layers of the procuticle (L2; Fig. 5A).

Our results suggest the following hypothesis. During early scale development, the outer layers of chitin-free epicuticle establish the ridges and the lower lamina. Chitin fibers are then produced during procuticle formation, but due to the inherent differences in the shapes of the upper vs lower laminas (buckled ridges vs a flat lower lamina), packing and cross-linking of the fibers with proteins may be different between the two layers. Chitin may be more densely packed in the flat lower lamina, leading to higher mass densities. Additionally, organization and cross-linking of the chitin fibers in the protein matrix potentially start earlier in the ridges and lower lamina compared to the cross-ribs and trabeculae. When pigments get incorporated at later stages of development, these pigment molecules have more spaces to infiltrate the more porous upper lamina sub-structures and may

modulate the polymerization of chitin and proteins to a greater extent in the late upper lamina sub-structures (cross-ribs and trabeculae) compared to the lower lamina. Though the lower lamina receives the same amount of pigment molecules, due to the lack of porosity, the pigment molecules may not infiltrate the densely packed chitin matrix as much as in the upper lamina and may settle on top, forming the innermost layer of the lower lamina (L1; Fig. 5A). Numerous examples of adsorbants and small molecules controlling nanocrystal growth have been established in the material sciences[45]. Pigment molecules like melanins might play similar roles in modulating chitin polymerization, and in differentiating rod-like and sheet-like structures.

Parameters other than pigmentation, however, may also regulate the variable cuticular density and morphology observed in the cross-ribs. Sheet-like cross-ribs developed in the less pigmented scales of both species (Figs. S5, S6), but while the cross-ribs in the lighter *yellow B. anynana* mutant were denser than those in the darker wildtype scale (Figs. 4C, D, S11), the opposite was seen for the lighter *J. orithya* male cross-ribs relative to those of the darker female scale (Fig. 4A, B). It is possible that distinct cuticular proteins, or even different pigments, used by each species contribute to further regulate cuticle density and morphology of the cross-ribs.

In conclusion, by studying two pairs of differentially pigmented scales in two different species of butterflies, we analyzed the broad distribution of pigmentation and its influence on scale structure and structural color. We identified that scales, just like other bio-composite materials such as wood and bone[46], exhibit variations in morphologies, structure, and composition across nanometer to micrometer ranges. Such hierarchical structuring provides multifunctionality at various structural levels by careful tuning of the material properties. We believe that the future to understanding the diversity of optical and mechanical properties of biomaterials will require 3D characterization of nanoscale variations in material composition, which quantitative density mapping techniques like PXCT, spectro-ptychography, and Atomic Force Microscopy (AFM), complementing the traditional imaging modalities, can help uncover.

Methods

Specimens
Individuals of wildtype *Bicyclus anynana* butterflies were sampled from the stock population in the Monteiro lab. A mutant *yellow* line was generated by a CRISPR/Cas9 knockout of the gene *yellow*[47]. Individuals of *Junonia orithya* were collected from Coney Island, Singapore (Permit No: NP/RP 14-063-2) and were placed in mesh cages with the host plant, *Asystasia gangetica*, to collect eggs. They were fed with 5% sugar water, and additional sources of heat were added to elicit activity. Caterpillars were reared for one generation in a 27 °C temperature-controlled room with a 12:12 h light cycle and 65% humidity.

Optical imaging
Epi-illumination microscope images of individual scales (Fig. 1) were obtained with a 20x lens of a uSight-2000-Ni microspectrophotometer (Technospex Pte. Ltd., Singapore) and a Touptek U3CMOS-05 camera. Images at different depths were obtained and computationally stacked using Adobe Photoshop v 22.5.1 (Adobe, California, USA). High-resolution epi-illumination images of the *J. orithya* male scale in Fig. 5, were obtained with a 100x lens of a Nikon ECLIPSE LV100ND microscope and a DS-Fi3 camera. Images at different depths were obtained and computationally stacked with the custom python code.

UV-VIS-NIR microspectrophotometry
Reflectance and absorbance measurements from individual scales were captured with a 20x objective (NA = 0.5) from a - 2 μm sized spot using a uSight-2000-Ni microspectrophotometer (Technospex Pte. Ltd., Singapore). Illumination was from a Mercury-Xenon lamp

(ThorLabs Inc., New Jersey, USA). Due to the glass microscope objective, the microspectrophotometer spectra were unreliable for wavelengths in the UV range (< 350 nm). The reflectance measurements were taken from five different scales of *J. orithya* male (blue) and four different scales of female (brown), two scales of *B. anynana* wildtype, and a single scale of *B. anynana yellow* mutant. The absorbance measurements were taken from two different scales of *J. orithya* male (blue) and a single scale of *J. orithya* female (brown), *B. anynana* wildtype, and *yellow* mutant. All the scales are collected from a single individual of each type. Since we plotted the average reflectance curves from multiple scales with shifted peaks in the reflectance data, the reflectance curves are dimmer and bi-modal in Fig. 1D'-E'.

To remove the upper lamina, the scales were placed on a glass slide, and another glass slide was placed on top to partly cover each scale. The upper lamina in the exposed regions of the scales was scraped off with a pin, and the debris was removed using sticky tape. An SEM image and an optical image of a scale with regions of intact and cleanly peeled off upper lamina are shown in Fig. 1F. For the reflectance measurements, we used a mirror as a reference (made of polished aluminum, manufactured in the Singapore University of Technology and Design) because the lower lamina of scales are specular reflectors. As the mirror reference reflects all the incident light, it can model reflectance quantitatively.

For the absorbance measurements, a drop of refractive index matching fluid (clove oil, Hayashi Pure Chemical Ind., Ltd.) was added on top of the lower lamina removed scales, and covered with a cover slip (Fig. S1). The region under the cover slip with no scale was used as a reference for absorbance measurements. Analysis and spectral plots were done in R Studio 1.4.1106 with R 4.0.4[48] using the R-package *pavo* (v 2.7)[49].

Scanning electron microscopy (SEM) and scale measurements
Three to six individual scales were sampled from the different areas under study from five different individuals and placed on carbon tape. Samples were processed in one of two ways: a) sputter-coated with gold using a JFC-1100 Fine Coat Ion Sputter (JEOL Ltd. Japan) and imaged using a JEOL JSM-6510LV scanning electron microscope (JEOL Ltd. Japan) or b) sputter-coated with platinum using a JFC-1600 Auto Fine Coater (JEOL Ltd. Japan) and imaged using a JEOL JSM-6701F FESEM (JEOL Ltd. Japan).

All measurements were done using ImageJ 1.53p[50]. For inter-ridge distance measurements, five individual measures were taken for each scale and averaged. Cross-rib distances were calculated by measuring the number of cross-ribs per 15 μm.

Statistical analysis
Analyses were done on R Studio 1.4.1106 with R 4.0.4[48]. Since the datasets were hierarchical with many scales sampled from each individual, the differences in mean values of inter-ridge and cross-rib distances among the different comparisons were modeled using a linear mixed-effects model (lme). This type of model allows for fixed and random effects where we considered Sex (*J. orithya* male or female) and Type (*B. anynana* WT or *yellow* mutant) as fixed factors and scale nested within individual as a random factor. The linear mixed-effects model was run using the nlme package (v 3.1.152)[51]. To address the violation of the homogeneity of variance in certain measurements, we used the 'varIdent' function in the nlme package to allow for different variance structures. Models were compared using the ANOVA function, and the best models were selected using the Akaike Information Criterion.

Focused ion beam scanning electron microscopy (FIB-SEM) and thickness measurements
Lower lamina thickness of all four scale types was measured using FIB-SEM. Measurements were corrected for tilt by dividing the values by

sin 52°. Samples were first sputter-coated with platinum, then milled at the center of each scale using a gallium ion beam on a FEI Versa 3D. The following settings were used: beam voltage −8 kV, beam current −12pA at a 52° tilt. Images were acquired with the following settings: beam voltage −5 kV, beam current −13pA. Five scales were sampled from a single individual of each category. For each scale, ten measurements of thickness were taken along the cross-section of the lower lamina using Fiji 1.53p[50].

Ptychographic X-ray computed tomography (PXCT)

In preparation for the tomographic X-ray imaging, one scale of each scale type of both *J. orithya* and *B. anynana* were fixed at the tip of a sharp needle (0.4 mm diameter at the base), which was then inserted into a 0.5 mm hole drilled at the center of a standard SEM specimen stub (12.5 mm diameter, 3.2 x 8 mm pin). Additionally, the needle was glued to the stub at its base. The PXCT data was collected at the I13−1 Coherent Branchline[52–54] at the Diamond Light Source with a photon energy of 9.7 keV, similar to a previous experiment on butterfly scales[35]. The sample plane was located ~14 mm downstream of the focal plane of the X-ray beam providing a defocused beam with a diameter of ~13 um. Focusing was achieved using a Blazed Fresnel zone plate (courtesy of collaboration with C. David/PSI) with 400 um diameter and 150 nm outer zone width. The data for the male specimen of *J. orithya* was collected with the Merlin detector, all other specimens were collected with the EXCALIBUR detector[55,56]. Both detectors are based on Medipix3 arrays with 55 um pixel pitch, and they were both located 14.65 m downstream of the sample plane. For each PXCT measurement, the specimen stub was mounted at the center of the translational and rotational sample stage and scanned transversally with a step size of 4 um for 1250 equally spaced tomographic angles between 0° and 180° providing a ptychographic dataset for each tomographic angle. The ptychographic data was reconstructed using 1000 iterations of the semi-implicit Douglas-Rachford algorithm[57] with sigma = 0.5 and tau = 0.1 as implemented in the PtyPy framework[58]. As a pre-processing step, all diffraction patterns were cropped to 512 × 512 pixels resulting in a reconstructed pixel size of 66.5 nm in the given experimental geometry, and a bad pixel mask (including hot, dead, inactive pixels) was used. The initial guess for the illumination was determined by collecting and reconstructing data from a Siemens star test target. For each specimen a tomographic volume was reconstructed based on the ptychographic phase projections using the filtered-back projection algorithm (Ram-Lak filter) from the ASTRA toolbox[59] as implemented in the Savu framework[60]. Prior to the tomographic reconstruction, the phase projections were aligned along the vertical direction by correlating integrated vertical line profiles[61], and the center of rotation was determined using a simplified version of this method[62] with a manual search instead of the Fourier analysis. To improve the quality of the tomographic reconstructions, the volume was forward-projected to generate a set of synthetic phase projections. These synthetic phase images were compared against the original phase reconstructions while searching for an improved alignment in both the vertical and horizontal directions[61,63]. The updated phase projections were subsequently put through the same tomographic reconstruction process as described above. This iterative alignment scheme was repeated 5 times providing a total of 4 three-dimensional electron density maps (Fig. 3).

Segmentation and mass density estimation

We used a series of computational techniques to process the reconstructed volumes from PXCT to extract quantitative data effectively. We illustrate the density estimation procedure with a detailed step-by-step schematic in Fig. 6, using a small cross-section of the PXCT reconstructed volume of *J. orithya* blue male scale (Fig. 6A). The reconstructed volumes were first rotated such that the lower lamina aligns flat (as much as possible) on the *x-y* plane (Fig. 6B). This rotation

was performed using a combination of principal component analysis (PCA) on selected features of each scale. Each rotated scale was inspected to ensure that the lower lamina was satisfactorily aligned to the *x-y* plane. Then we used a peak finding method to find the dense lower lamina along 1D *z*-axis phase profiles (i.e., constant *x,y*) of the 3D phase volume (i.e., electron density) obtained from PXCT (Fig. 6C). Once the lower lamina was located, it was digitally translated in *z* to remove local undulations (tilt variations) (Fig. 6D). This translation reduced the variations in distances between the lower lamina to upper lamina features (e.g., ridges and/or cross-ribs). This variation reduction assisted the segmentation and classification of features on the upper lamina. However, the upper lamina structures are neither continuous nor feasible to align. Hence, we needed a clustering method to classify the substructures in the upper lamina. The 1D curves were classified based on the (non-exclusive) presence of the following features: lower lamina, ridges, cross-ribs, and trabeculae. PCA dimensionality reduction (5 principal components) was carried out on 1D *z*-axis phase profiles, followed by feature vectorization using K-means clustering. We increased the number of clusters in the analysis based on the complexity and the reconstruction quality of the volume. For noisy and complex volumes, we manually labeled the K-means clusters further into ridges, cross-ribs, trabeculae and discarded obvious outliers (Fig. 6E). The visual validation for our clustering is shown in Fig. 3A''–D'' and a cross-sectional view in Fig. 6E. However, for completeness, we carried out a t-distributed Stochastic Neighbor Embedding (t-SNE) dimensionality reduction on the PCA components to visualize the inter-cluster separation (Fig. S12A), and an adjusted pairwise mutual information score was calculated to evaluate the K-means clustering (Fig. S12B). Although t-SNE analysis shows that the clusters were not well separated, the adjusted mutual information values, which are closer to 1, showed that our clustering was consistent and repeatable. The average 1D profiles of these upper and lower lamina features in a particular cluster are shown in Fig. 3A–D.

After classification, each of these upper and lower lamina substructures (represented by index *c*) were separately fitted to 1D Gaussians to infer the average densities ($\rho_{x,y,c}$), *z*-axis thickness ($t_{x,y,c}$), and *z*-position of these features. The Gaussian model was chosen as it accurately approximates the densities affected by the tomographic artifacts (Figs. 3A, 6F). It is noteworthy that the 1D profiles dip slightly into negative values due to reconstruction artifacts from tomographic stitching. While such artifacts are common[64], in this analysis, we did not allow the fitted 1D Gaussians to be negative. Hence, these 1D Gaussian fits also reduced artifacts from tomographic stitching and noise. In the case of *B. anynana yellow* mutant scale, a double Gaussian was used for the upper lamina, instead of a single Gaussian, to account for its complex structure (tilted trabeculae beneath the ridge), in addition to a separate Gaussian fitted for the lower lamina. From these fits, the area under the Gaussians provides the phase sum along the *z*-axis ($\varphi_{x,y,c}$), and twice the standard deviation ($2\sigma_{x,y,c}$), of the Gaussians provides the thickness along the *z*-axis ($t_{x,y,c}$). We calibrated these PXCT thicknesses based on the *J. orithya* male scale's lower lamina's experimental thickness measurement (SEM and TEM) and applied the same to determine the thickness values for all the substructures of every scale. The phase sum and the thickness values are then used to calculate the integrated electron density along the z-axis for each pixel at the x-y plane[65]. With the electron density of a chitin monomer (e^-_{chitin}) and the x-ray wavelength (λ_X), we converted the phase sum into an estimate of the total number of chitin monomers. The mass density ($\rho_{x,y,c}$) of each component at a given substructure (1D profiles) was calculated by using the molecular mass of a chitin monomer (m_{chitin}) and Avogadro's number (N_A) (Eq. 1).

$$\rho_{x,y,c} = \left(\frac{\varphi_{x,y,c}}{t_{x,y,c}} \right) \left(\frac{m_{chitin}}{r_e \lambda_X N_A e^-_{chitin}} \right) \tag{1}$$

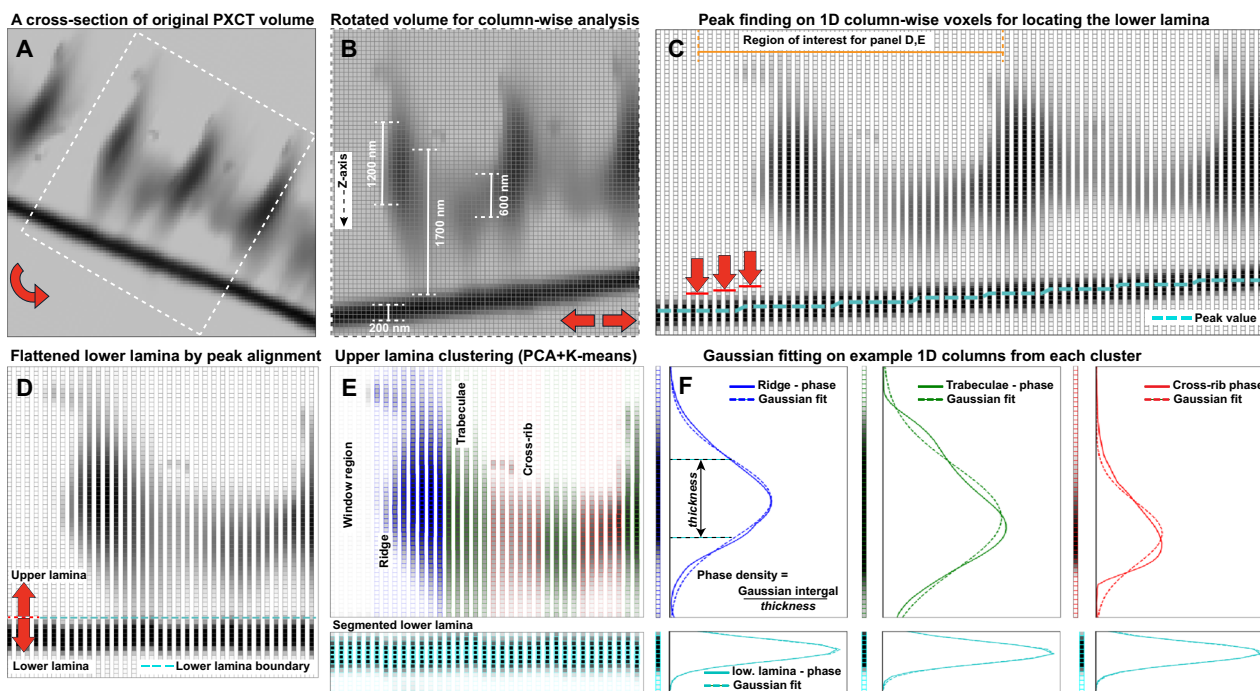**Fig. 6 | PXCT density estimation schematic. A** A 2D cross-section of the PXCT reconstruction volume of a blue scale of *J. orithya* male; the boxed region is selected for the demonstration. Each voxel's reconstructed phase density is shown in grayscale (darker means denser). Red arrows in each panel indicate the next key transformation step. In this panel, the red arrow shows the rotation direction of the volume (**B**). The volume is rotated by the global mean tilt so that the lower lamina of the entire scale (which extends beyond this field of view) is, as much as possible, aligned with the *x-y* plane. Consequently, the trabeculae are conveniently aligned along the vertical *z*-axis for column-wise analysis. Red arrows indicate that the volume will be laterally partitioned into multiple 1D (*z*-axis) voxel columns next. **C** Using peak-finding, we separately detect the position of the lower lamina in each 1D column (indicated by cyan markers). Red arrows indicate that these detected

peaks will be computationally aligned in the next step, since we cannot remove the local undulations in the lower lamina of the entire scale with a single rotation. **D** Local undulations in the lower lamina are flattened via peak alignment. Red arrows indicate that the lower lamina will be segmented from the upper lamina features within each 1D column in the next step. **E** The upper lamina feature vectors are reduced and clustered into four categories—window, ridge, trabeculae, and cross-rib—using PCA followed by K-means clustering. **F** The 1D profiles of the lower lamina and the upper lamina features of each column are then fitted to Gaussian functions to reduce partial volume effects and estimate thickness and phase density. This fitting is separately done on every 1D column throughout the volume. Shown here are examples from one column per cluster (ridge, trabeculae, and cross-rib).

We emphasize that our absolute mass density estimates obtained with PXCT are based on the average ratio of electron-to-nucleon in chitin ($C_8H_{13}O_5N$) only, because the cuticular protein and pigment composition within the scales are unknown. Hence, estimates of absolute densities would increase by 11%, had we recalibrated for melanin pigment monomers instead ($C_{18}H_{10}O_2N_2$). Nevertheless, the relative differences in the average mass densities between upper and lower laminas in all four scales in Fig. 4 exceed this 11% difference due to calibration choice. Consequently, the density differences between the most prominent features in the lower and upper laminas cannot be explained by a (highly unlikely) replacement of all chitin monomers entirely with melanin monomers. Since the ratio of electron-to-nucleon of a chitin monomer and a chitin polymer is identical, we used the monomer's chemical composition in our calculations for convenience.

Step-by-step procedural description of mass density estimation

1. The PXCT reconstructed volume is rotated such that the lower lamina aligns with the *x-y* plane (Fig. 6B).
2. Further, a peak finding on 1D curves along the *z*-axis at every *x-y* position is carried out to determine the position of the lower lamina (Fig. 6C).
3. The lower lamina is digitally flattened to remove all the local undulations by aligning the peaks determined from the previous step (Fig. 6D).
4. Since the upper lamina is not continuous, PCA and K-means are applied to cluster the 1D curves to segment the volume and

identify the substructures of the upper lamina. We employed five PCA components and four clusters for K-means. We increased the number of clusters for scales with complex structures and validated the clustering with t-SNE (Fig. 6E).

5. After segmentation, Gaussian fitting is employed on every single 1D curve of each cluster (c) to determine the average lower bound estimates of the mass density (Fig. 6F). The Gaussian fitting ensures the estimates are more robust against the tomographic artifacts and better than the direct voxel-wise estimation (Fig. S8).
6. The area under the Gaussian curve provides the phase sum along the *z*-axis ($\varphi_{x,y,c}$) (Fig. 6F).
7. From TEM and SEM thickness measurements, the thickness along the *z*-axis is calibrated as twice the value of the fitted standard deviation ($t_{x,y,c} = 2\sigma_{x,y,c}$).
8. The phase sum and the thickness can already provide the average electron density of each 1D profile.
9. Based on the assumption that the material is chitin (to convert electron to nucleon density), the mass density is estimated from the phase sum and thickness using Eq. 1.
10. The partial volume effect and the presence of melanin, which has an 11% higher nucleon-to-electron ratio than chitin, render our mass density estimates to be the lower bound.

Partial volume effect

The mass density estimations of the sub-structures should be inferred cautiously as they suffer from the partial volume effect, i.e., a limited resolution of an imaging system underestimates the density in smaller

features. For example, the ectopic cuticular film of *B. anynana yellow* mutant scale is thinner than a PXCT voxel; thus, the electron mass reported in that voxel is averaged over the larger voxel size instead of the actual thickness of the upper lamina, which causes a lower density than the actual value. Though significant in the case of the thin ectopic film, all the other features (cross-ribs, ridges, trabeculae, and lower lamina) that are larger than two voxels are less affected by the partial volume effect[66]. Conservatively, all the mass density values estimated should be considered as the lower bound of the actual densities. However, the relative change in densities of sub-structures within a scale (except for the ectopic film) and densities of the same structure between different scales can be inferred with confidence since the voxel size is the same in all reconstructions. It is noteworthy that the partial volume effect can be substantially reduced by collecting PXCT data with a higher resolution (i.e., by increasing exposure times at the expense of longer data acquisition times); hence it is not an innate limitation of PXCT or the mass density estimation.

Optical modeling

The reflectance spectrum from a scale is a collective product of a series of optical responses from the structure. Numerical methods can simulate the complete response spectrum from a given 3D structure. However, they are computationally expensive for carrying out multiple simulations that are required for parameter tuning to fit the experimental response curves. Here we used an analytical model where an incident spectrum reflected back from the lower lamina at various layers interfere to produce a response reflection spectrum. We used the scattering matrix (S-matrix) method to calculate a reflectance spectrum from the lower lamina as we can model multi-layered lower lamina (N layers) with this method[67]. Scattering matrix implementation in the PyPI python library has been used, and we calculated the reflection and transmission intensity (Eq. 2) for every wavelength data point from the experiment.

$$\left[I_{ref}(\lambda)I_{trn}(\lambda)\right] = S^{ll}(0,N)\left[I_{inc}(\lambda)0\right] \qquad (2)$$

We implemented a *Python* fitting routine that uses our optical model to fit the wavelength-dependent refractive indices of each layer by minimizing the difference between the model output and the experimentally measured reflectance data.

We modeled a four-layer lower lamina with the layer thickness obtained from the TEM cross-section (Fig. 5A). Further, we accounted for the absorbance, the numerical aperture, and the local thickness variation (obtained from the SEM measurements) to fit the Cauchy coefficients for each layer, which represent the wavelength-dependent refractive indices. The scales with reflectance and absorbance measurements were used for the modeling (Fig. S9B, C). First, we corrected the experimental reflectance spectra to compensate for the absorbance with the corresponding absorbance measurements (Fig. S9D). We defined a probability distribution of thicknesses obtained from the mean and variance of thickness from the SEM measurements to simulate the local thickness variation (Fig. S9E). Then, we estimated the half-angle (30°) for the cone of the incident light from the numerical aperture (0.5). Our model integrates the thin-film reflectance response from the thickness and the incident angle distribution (0 to 30°) to obtain the final reflectance spectra (Fig. S9F). Since the upper-lamina-removed scales were fragile, it was difficult to move them to a black tape for the reflectance measurement and bring them back to a glass slide for the absorbance measurement without damaging the scale. Hence, we measured the reflectance of the scale on top of a glass slide. To be thorough, we have also included the glass substrate background and a thin air gap (<5 nm) between the scale and the glass slide in our model (Fig. 5D). Since we used the mirror reference for the measurements and included the glass substrate in our model,

we did not require to normalize the spectra nor a correction factor to account for the overestimation.

Absorption spectrum and pigment concentration estimation

Spectrophotometer measures absorbance $A(\lambda, t)$ from the fraction of the light transmitted $T(\lambda, t)$ through a sample of thickness t as a function of the wavelength of incident light λ. This absorbance is shown in Eq. (3)

$$A(\lambda, t) = -\log_{10} T(\lambda, t). \qquad (3)$$

In the case of butterfly scales, this absorbance is affected by the *types* and *density* of light-absorbing pigments within the scale, as well as the scale's thickness. Hence, to compare the density of pigments within different regions of a scale (i.e., upper versus lower lamina) and between similar scales, we need to account for the corresponding thicknesses of pigment-containing features within the scale. Fortunately for us, this thickness information can be inferred from SEM and PXCT measurements.

The SEM cross sections of the four types of scales presented in this manuscript each show relatively little variations in the thickness of their lower lamina (Figs S5, S6). Unlike the lower lamina, however, the upper lamina of each of these four scale types contain a complex structure with ridges, cross-ribs, trabeculae and window regions. Hence, the probability distribution of thicknesses across such a complex structure should be estimated for its transmittance model. For each scale, we estimated the thickness distribution of its upper lamina from 100 randomly sampled 2 μm-diameter patches from its corresponding PXCT reconstruction volume. This diameter was chosen to match the illumination spot sizes using in the micro-spectrophotometry measurements (described in an earlier section in the methods).

Overall, the average transmittance for such an upper and lower lamina structure can be modeled using the following pair of Beer-Lambert law:

$$T_{U+L}(\lambda) = e^{-(\mu_L(\lambda)t_L)} \sum_{t_U} \Pr(t_U) e^{-(\mu_U(\lambda)t_U)} \qquad (4)$$

$$T_L(\lambda) = e^{-(\mu_L(\lambda)t_L)} \qquad (5)$$

where $\mu_L(\lambda)$, $\mu_U(\lambda)$, and t_L, t_U are pairs of absorption spectra and thickness of the lower and upper lamina, respectively. $\Pr(t_U)$ is the probability distribution of the upper lamina thickness (from PXCT reconstruction), which allows us to account for the varying thicknesses of the upper lamina features in each scale. These thickness values t_L were calibrated based on the thickness of the lower lamina experimentally measured from the SEM, which is more precise than that from PXCT.

To reduce the partial volume effect from upper lamina feature thicknesses (t_U) inferred from PXCT, we found the scaling factor needed to match the lower lamina thicknesses between PXCT and SEM measurements for each scale. This butterfly-scale-dependent scaling factor was used to rescale each scale's upper lamina thickness distribution to minimize the partial volume effect.

Here's what we did, in detail. For each scale, whose lower-lamina thickness t_L was measured via SEM, we fitted its measured lower-lamina-only absorbance $T_L(\lambda)$ to Eq. (5) to find the absorption spectra of the lower lamina $\mu_L(\lambda)$. These fitted parameters were substituted into Eq. (4), together with the upper lamina thickness distribution $\Pr(t_U)$ from PXCT (after correcting for partial volume effects) and fitted to the upper-plus-lower lamina microphotospectra absorbance $T_{U+L}(\lambda)$. Doing this gave us the absorption spectra of just the upper lamina $\mu_U(\lambda)$.

Notice that now that we have the thickness-independent absorption spectra of the upper and lower laminas (i.e., $\mu_U(\lambda)$ have $\mu_L(\lambda)$), we can determine the chemical signature and density of the pigments in each. To facilitate this, we decomposed the absorption spectrum $\mu(\lambda)$ into two independent parts:

$$\mu(\lambda) = c\varepsilon(\lambda) \qquad (6)$$

where c is the molar concentration of the light-absorbing pigments and $\varepsilon(\lambda)$ is the molar absorption spectrum of these pigments. Should the upper and lower laminas have comparable wavelength dependence of $\varepsilon(\lambda)$ (i.e., $\varepsilon_U(\lambda)/\varepsilon_L(\lambda)$ is a wavelength-independent constant) we can be more confident in asserting that they contain the same type of pigments, except at different relative concentrations. Fig. S2 shows the molar absorption spectrum $\varepsilon(\lambda)$ for the upper and lower lamina of four scales studied here (that of the lower lamina of *J. orithya* male was omitted because it was too noisy). Fig. S2 also compares the relative molar concentrations of pigments in these scales.

Transmission electron microscopy of resin-embedded scales

Small pieces of each wing section were cut and fixed in 2.5% Glutaraldehyde in (Phosphate-buffered saline) PBS overnight at 4 °C followed by three washes in PBS. Samples were then processed at the Electron Microscopy Unit at the Yong Loo Lin School of Medicine, NUS. Briefly, samples were post-fixed in 1 or 2% OsO4, pH7.4 for 1 h at room temperature under a fume hood and washed in deionized water for 10 min for 2 changes at room temperature. Dehydration was through an ascending ethanol series at room temperature: 25% ethanol for 5 min, 50% and 75% ethanol for 10 min, 95% and 100% ethanol for 20 min. Samples were then transferred to 100% acetone for 20 min, 2 times. Infiltration was with the following steps: a) 100% acetone: Araldite resin (3:1) for 30 mins at room temperature b) 100% acetone: Araldite resin (1:1) for 1 h at room temperature c) 100% acetone: Araldite resin (1:6) for overnight at room temperature d) Pure Araldite resin for 30 min at room temperature then for 30 min in a 40 °C oven e) Change to pure Araldite resin again for 1 h in a 45 °C oven f) Last change to pure Araldite resin for 1 h in a 50 °C oven. Finally, samples were embedded in fresh resin and allowed to polymerize for 24 h in a 60 °C oven. For some *J. orithya* male samples, no post-fixation in OsO4 was carried out.

Ultrathin sections were cut using a Leica Ultracut UCT Ultramicrotome (Leica Microsystems, Germany) and transferred to formvar-coated grids. For the *J. orithya* samples grids were either left unstained or stained with lead citrate. For the *B. anynana* samples, all grids were stained with lead citrate. Images were acquired on a FEI Technai T12 Transmission Electron Microscopy (FEI, Thermo Fisher Scientific, USA).

Reporting summary

Further information on research design is available in the Nature Portfolio Reporting Summary linked to this article.

Data availability

Source data for all reflectance, absorbance, and thickness measurements are provided with this paper in Supplementary Data 1 and Supplementary Data 2 (Excel files). Cropped PXCT volumes used for segmentation and density analysis are openly available in Zenodo (https://doi.org/10.5281/zenodo.12703866)[68]. The full reconstructed PXCT volumes and corresponding raw data are not publicly hosted due to file-size constraints; they are available upon request via email to the corresponding author.

Code availability

The custom codes (Jupyter notebooks) for X-ray psycho-tomography 3D volumetric data analysis and optical modeling are available in the same Zenodo repository (https://doi.org/10.5281/zenodo.12703866)[68].

References

1. Miserez, A., Schneberk, T., Sun, C., Zok, F. W. & Waite, J. H. The transition from stiff to compliant materials in squid beaks. *Science* **319**, 1816–1819 (2008).
2. Eliason, C. M. & Shawkey, M. D. A photonic heterostructure produces diverse iridescent colours in duck wing patches. *J. R. Soc. Interface* **9**, 2279–2289 (2012).
3. Craig, A. J. F. K. & Hartley, A. H. The arrangement and structure of feather melanin granules as a taxonomic character in African starlings (Sturnidae). *Auk* **102**, 629–632 (1985).
4. Moussian, B., Seifarth, C., Müller, U., Berger, J. & Schwarz, H. Cuticle differentiation during *Drosophila* embryogenesis. *Arthropod Struct. Dev.* **35**, 137–152 (2006).
5. Noh, M. Y., Muthukrishnan, S., Kramer, K. J. & Arakane, Y. Cuticle formation and pigmentation in beetles. *Curr. Opin. Insect Sci.* **17**, 1–9 (2016).
6. Politi, Y., Bertinetti, L., Fratzl, P. & Barth, F. G. The spider cuticle: a remarkable material toolbox for functional diversity. *Philos. Trans. R. Soc. A Math. Phys. Eng. Sci.* **379**, 20200332 (2021).
7. Willis, J. H. Structural cuticular proteins from arthropods: annotation, nomenclature, and sequence characteristics in the genomics era. *Insect Biochem. Mol. Biol.* **40**, 189–204 (2010).
8. Xiong, G. et al. Body shape and coloration of silkworm larvae are influenced by a novel cuticular protein. *Genetics* **207**, 1053–1066 (2017).
9. Liu, J. et al. Lepidopteran wing scales contain abundant cross-linked film-forming histidine-rich cuticular proteins. *Commun. Biol.* **4**, 491 (2021).
10. Tajiri, R., Ogawa, N., Fujiwara, H. & Kojima, T. Mechanical control of whole body shape by a single cuticular protein obstructor-E in *Drosophila melanogaster*. *PLoS Genet.* **13**, 1–26 (2017).
11. Arakane, Y. et al. Formation of rigid, non-flight forewings (Elytra) of a beetle requires two major cuticular proteins. *PLoS Genet.* **8**, e1002682 (2012).
12. Noh, M. Y., Muthukrishnan, S., Kramer, K. J. & Arakane, Y. *Tribolium castaneum* RR-1 cuticular protein TcCPR4 is required for formation of pore canals in rigid cuticle. *PLoS Genet.* **11**, e1004963 (2015).
13. Noh, M. Y. et al. Two major cuticular proteins are required for assembly of horizontal laminae and vertical pore canals in rigid cuticle of *Tribolium castaneum*. *Insect Biochem. Mol. Biol.* **53**, 22–29 (2014).
14. Politi, Y. et al. A spider's fang: how to design an injection needle using chitin-based composite material. *Adv. Funct. Mater.* **22**, 2519–2528 (2012).
15. Locke, M. The wigglesworth lecture: insects for studying fundamental problems in biology. *J. Insect Physiol.* **47**, 495–507 (2001).
16. Chandran, R., Williams, L., Hung, A., Nowlin, K. & LaJeunesse, D. SEM characterization of anatomical variation in chitin organization in insect and arthropod cuticles. *Micron* **82**, 74–85 (2016).
17. Raabe, D. et al. Microstructure and crystallographic texture of the chitin-protein network in the biological composite material of the exoskeleton of the lobster *Homarus americanus*. *Mater. Sci. Eng. A* **421**, 143–153 (2006).
18. Raabe, D., Sachs, C. & Romano, P. The crustacean exoskeleton as an example of a structurally and mechanically graded biological nanocomposite material. *Acta Mater.* **53**, 4281–4292 (2005).
19. Sviben, S. et al. Epidermal cell surface structure and chitin-protein co-assembly determine fiber architecture in the locust cuticle. *ACS Appl. Mater. Interfaces* **12**, 25581–25590 (2020).
20. Yu, R. et al. Helicoidal organization of chitin in the cuticle of the migratory locust requires the function of the chitin deacetylase2 enzyme (LmCDA2). *J. Biol. Chem.* **291**, 24352–24363 (2016).
21. Ghiradella, H. Structure of butterfly scales: patterning in an insect cuticle. *Microsc. Res. Tech.* **27**, 429–438 (1994).

22. Stavenga, D. G., Leertouwer, H. L. & Wilts, B. D. Coloration principles of nymphaline butterflies - thin films, melanin, ommochromes and wing scale stacking. *J. Exp. Biol.* **217**, 2171–2180 (2014).

23. Zhang, L. et al. Genetic basis of melanin pigmentation in butterfly wings. *Genetics* **205**, 1537–1550 (2017).

24. Ghiradella, H. Light and color on the wing: structural colors in butterflies and moths. *Appl. Opt.* **30**, 3492–3500 (1991).

25. Ghiradella, H. T. & Butler, M. W. Many variations on a few themes: a broader look at development of iridescent scales (and feathers). *J. R. Soc. Interface* **6**, S243–S251 (2009).

26. Dinwiddie, A. et al. Dynamics of F-actin prefigure the structure of butterfly wing scales. *Dev. Biol.* **392**, 404–418 (2014).

27. Overton, J. Microtubules and microfibrils in morphogenesis of the scale cells of *Ephestia kühniella*. *J. Cell Biol.* **29**, 293–305 (1966).

28. Ghiradella, H. Development of ultraviolet-reflecting butterfly scales: how to make an interference filter. *J. Morphol.* **142**, 395–409 (1974).

29. Koch, P. B., Lorenz, U., Brakefield, P. M. & ffrench-Constant, R. H. Butterfly wing pattern mutants: developmental heterochrony and coordinately regulated phenotypes. *Dev. Genes Evol.* **210**, 536–544 (2000).

30. Thayer, R. C., Allen, F. I. & Patel, N. H. Structural color in *Junonia* butterflies evolves by tuning scale lamina thickness. *Elife* **9**, e52187 (2020).

31. Matsuoka, Y. & Monteiro, A. Melanin pathway genes regulate color and morphology of butterfly wing scales. *Cell Rep.* **24**, 56–65 (2018).

32. Livraghi, L. et al. *Cortex cis*-regulatory switches establish scale colour identity and pattern diversity in *Heliconius*. *Elife* **10**, 1–31 (2021).

33. Dierolf, M. et al. Ptychographic X-ray computed tomography at the nanoscale. *Nature* **467**, 436–439 (2010).

34. Holler, M. et al. High-resolution non-destructive three-dimensional imaging of integrated circuits. *Nature* **543**, 402–406 (2017).

35. Sala, S. et al. Ptychographic X-ray computed tomography at a high-brilliance X-ray source. *Opt. Express* **27**, 533–542 (2019).

36. Singer, A. et al. Domain morphology, boundaries, and topological defects in biophotonic gyroid nanostructures of butterfly wing scales. *Sci. Adv.* **2**, e1600149 (2016).

37. Wilts, B. D. et al. Evolutionary-optimized photonic network structure in white beetle wing scales. *Adv. Mater.* **30**, 1702057 (2018).

38. Dougherty, G. & Newman, D. Measurement of thickness and density of thin structures by computed tomography: a simulation study. *Med. Phys.* **26**, 1341–1348 (1999).

39. Trzeciak, T. M., Wilts, B. D., Stavenga, D. G. & Vukusic, P. Variable multilayer reflection together with long-pass filtering pigment determines the wing coloration of papilionid butterflies of the *nireus* group. *Opt. Express* **20**, 8877–8890 (2012).

40. Leertouwer, H. L., Wilts, B. D. & Stavenga, D. G. Refractive index and dispersion of butterfly chitin and bird keratin measured by polarizing interference microscopy. *Opt. Express* **19**, 24061–24066 (2011).

41. Wilts, B. D. Brilliant biophotonics. *physical properties, pigmentary tuning & biological implications* (2013).

42. Stavenga, D. G., et al. Classical lepidopteran wing scale colouration in the giant butterfly-moth *Paysandisia archon*. *PeerJ* **6**, e4590 (2018).

43. Angermüller, S. & Fahimi, H. D. Imidazole-buffered osmium tetroxide: an excellent stain for visualization of lipids in transmission electron microscopy. *Histochem. J.* **14**, 823–835 (1982).

44. Drochmans, P. Electron microscope studies of epidermal melanocytes, and the fine structure of melanin granules. *J. Biophys. Biochem. Cytol.* **8**, 165–180 (1960).

45. Chen, M., Wu, B., Yang, J. & Zheng, N. Small adsorbate-assisted shape control of pd and pt nanocrystals. *Adv. Mater.* **24**, 862–879 (2012).

46. Dunlop, J. W. C. & Fratzl, P. Biological composites. *Annu. Rev. Mater. Res.* **40**, 1–24 (2010).

47. Connahs, H. et al. The *yellow* gene regulates behavioural plasticity by repressing male courtship in *Bicyclus anynana* butterflies. *Proc. R. Soc. B Biol. Sci.* **289**, 20212665 (2022).

48. R Core Team. R: A language and environment for statistical computing. R Foundation for Statistical Computing, Vienna, Austria. https://www.R-project.org/ (2021).

49. Maia, R., Gruson, H., Endler, J. A. & White, T. E. pavo 2: New tools for the spectral and spatial analysis of colour in r. *Methods Ecol. Evol.* **10**, 1097–1107 (2019).

50. Schneider, C. A., Rasband, W. S. & Eliceiri, K. W. NIH Image to ImageJ: 25 years of image analysis. *Nat. Methods* **9**, 671–675 (2012).

51. Pinheiro, J., Bates, D. & R-core. nlme: linear and nonlinear mixed effects models. (2021).

52. Kuppili, V. S. C. et al. Ptychotomography at DLS coherence beamline I13. *J. Phys. Conf. Ser.* **849**, 12031 (2017).

53. Cipiccia, S. et al. Multi-scale multi-dimensional imaging at I13-coherence branchline in diamond light source. *AIP Conf. Proc.* **2054**, 50005 (2019).

54. Rau, C., Wagner, U., Pešić, Z. & De Fanis, A. Coherent imaging at the Diamond beamline I13. *Phys. status solidi* **208**, 2522–2525 (2011).

55. Tartoni, N. et al. Excalibur: A three million pixels photon counting area detector for coherent diffraction imaging based on the Medipix3 ASIC. in 2012 IEEE Nuclear Science Symposium and Medical Imaging Conference Record (NSS/MIC) 530–533 (2012).

56. Marchal, J. et al. EXCALIBUR: a small-pixel photon counting area detector for coherent X-ray diffraction - Front-end design, fabrication and characterisation. *J. Phys. Conf. Ser.* **425**, 62003 (2013).

57. Pham, M., Rana, A., Miao, J. & Osher, S. Semi-implicit relaxed Douglas-Rachford algorithm (sDR) for ptychography. *Opt. Express* **27**, 31246–31260 (2019).

58. Enders, B. & Thibault, P. A computational framework for ptychographic reconstructions. *Proc. R. Soc. A Math. Phys. Eng. Sci.* **472**, 20160640 (2016).

59. van Aarle, W. et al. Fast and flexible X-ray tomography using the ASTRA toolbox. *Opt. Express* **24**, 25129–25147 (2016).

60. Wadeson, N. & Basham, M. Savu: A python-based, MPI framework for simultaneous processing of multiple, N-dimensional, large tomography datasets. *CoRR* **abs/1610.0**, (2016).

61. Guizar-Sicairos, M. et al. Phase tomography from x-ray coherent diffractive imaging projections. *Opt. Express* **19**, 21345–21357 (2011).

62. Vo, N. T., Drakopoulos, M., Atwood, R. C. & Reinhard, C. Reliable method for calculating the center of rotation in parallel-beam tomography. *Opt. Express* **22**, 19078–19086 (2014).

63. Gürsoy, D. Direct coupling of tomography and ptychography. *Opt. Lett.* **42**, 3169–3172 (2017).

64. Shen, K. et al. Negativity artifacts in back-projection-based photoacoustic tomography. *J. Phys. D. Appl. Phys.* **54**, 74001 (2021).

65. Chen, G.-H., Zambelli, J., Bevins, N., Qi, Z. & Li, K. X-ray phase sensitive imaging methods: basic physical principles and potential medical applications. *Curr. Med. Imaging Rev.* **6**, 90–99 (2010).

66. Kessler, R. M., Ellis, J. R. J. & Eden, M. Analysis of emission tomographic scan data: limitations imposed by resolution and background. *J. Comput. Assist. Tomogr.* **8**, 514–522 (1984).

67. Ko, D. Y. K. & Sambles, J. R. Scattering matrix method for propagation of radiation in stratified media: attenuated total reflection studies of liquid crystals. *J. Opt. Soc. Am. A* **5**, 1863–1866 (1988).

68. Balakrishnan, D. et al. Nanoscale cuticle density variations correlate with pigmentation and color in butterfly wing scales. *Zenodo* 10.5281/zenodo.12703866 (2024).

Acknowledgments

Author contributions

Conceptualization: A.P., B.J.D., A.M., and N.D.L. Methodology: D.B., A.P., B.J.D., P.T., A.M., and N.D.L. Formal analysis: D.B., B.J.D., Y.C.L., Z.S., and N.D.L. Investigation: D.B., A.P., B.J.D., C.F., and N.D.L. Visualization: D.B., A.P., and C.F. Funding acquisition: A.M., N.D.L., and P.T. Project administration: A.M. and N.D.L. Supervision: A.M. and N.D.L. Writing – original draft: D.B., A.P., and B.J.D. Writing – review & editing: D.B., A.P., B.J.D., C.F., P.T., A.M., and N.D.L.

Competing interests

The authors declare no competing interests.

Additional information

Supplementary information The online version contains supplementary material available at
https://doi.org/10.1038/s41467-025-62010-7.

Correspondence and requests for materials should be addressed to Antónia Monteiro or N. Duane Loh.

Peer review information *Nature Communications* thanks Bodo Wilts, and the other, anonymous, reviewer(s) for their contribution to the peer review of this work. A peer review file is available.

Reprints and permissions information is available at
http://www.nature.com/reprints

Publisher's note Springer Nature remains neutral with regard to jurisdictional claims in published maps and institutional affiliations.